



HAL
open science

Validation of 4D flow based relative pressure maps in the aorta

David Nolte, Jesús Urbina, Julio Sotelo, Leo Sok, Cristian Montalba, Israel Valverde, Axel Osses, Sergio Uribe, Cristobal Bertoglio

► To cite this version:

David Nolte, Jesús Urbina, Julio Sotelo, Leo Sok, Cristian Montalba, et al.. Validation of 4D flow based relative pressure maps in the aorta. 2020. hal-02113750v2

HAL Id: hal-02113750

<https://hal.science/hal-02113750v2>

Preprint submitted on 7 Jul 2020 (v2), last revised 28 Oct 2020 (v3)

HAL is a multi-disciplinary open access archive for the deposit and dissemination of scientific research documents, whether they are published or not. The documents may come from teaching and research institutions in France or abroad, or from public or private research centers.

L'archive ouverte pluridisciplinaire **HAL**, est destinée au dépôt et à la diffusion de documents scientifiques de niveau recherche, publiés ou non, émanant des établissements d'enseignement et de recherche français ou étrangers, des laboratoires publics ou privés.

Validation of 4D flow based relative pressure maps in the aorta

David Nolte^{1,4}, Jesús Urbina^{2,3}, Julio Sotelo², Leo Sok⁴, Cristian Montalba²
Israel Valverde⁷, Axel Osses^{1,5}, Sergio Uribe^{2,3,5}, Cristóbal Bertoglio^{4,1}

¹Center for Mathematical Modeling, Universidad de Chile

²Biomedical Imaging Center, Pontificia Universidad Católica de Chile

³Department of Radiology, School of Medicine, Pontificia Universidad Católica de Chile

⁴Bernoulli Institute, University of Groningen

⁵Millennium Nucleus for Cardiovascular Magnetic Resonance

⁶Department of Electrical Engineering, Pontificia Universidad Católica de Chile

⁷Hospital Universitario Virgen del Rocío, Sevilla, 41013, Spain

July 7, 2020

Abstract

Purpose: While the clinical gold standard for pressure difference measurements is invasive catheterization, 4D Flow is a promising tool for enabling a non-invasive quantification, by linking highly spatially resolved velocity measurements with pressure differences via the incompressible Navier–Stokes equations. In this work we provide a validation and comparison with phantom and clinical patient data of pressure difference maps estimators.

Methods: We compare the classical Pressure Poisson Estimator (PPE) and the new Stokes Estimator (STE) against catheter pressure measurements under a variety of stenosis severities and flow intensities. To validate both methods in controlled experiments, we include several 4D Flow data sets of realistic aortic phantoms with different anatomic and hemodynamic severities. To show the clinical applicability of both methods, we also include 4D Flow data sets of two patients with aortic coarctation (non repaired and repaired).

Results: The STE method, applied to high resolution in-vitro data including all investigated AoCo severities under rest and stress conditions, resulted in a RMSE in the pressure drop with respect to catheter measurements at peak systole of 5.85 mmHg, whereas the PPE method yielded a RMSE of 11.41 mmHg. On a segmentation with the lumen radius reduced by one voxel, the RMSE of the STE method was 5.00 mmHg and the RMSE of the PPE method was 9.01 mmHg. **Conclusion:** The STE method yields

more accurate results than the PPE method compared to catheterization data. The results indicate an improved robustness of the STE method with respect to variation in lumen segmentation.

Keywords: 4D Flow, pressure difference, catheter, PPE, STE, clinical and experimental validation

1 Introduction

Aortic coarctation (AoCo) is a narrowing of the proximal descending aorta, typically located at the aortic isthmus. AoCo accounts for 5–8% of all congenital heart defects (CHD) and the prevalence of isolated forms is 3 per 10000 live births [16]. The peak-to-peak pressure difference across the coarctation is the most important hemodynamic parameter for clinical decisions [46, 17].

In the clinical practice, different techniques are available to measure pressure differences across aortic coarctations. Catheterization is the gold standard technique, but is expensive, invasive, non-exempt of risk, the patient is exposed to X-rays and is difficult to reproduce. Doppler echocardiography using the simplified Bernoulli equation is the most available non-invasive method, but has certain limitations: it is operator dependent, has poor acoustic windows and spectral broadening, and in addition overestimates the peak velocities up to 25% [24]. Magnetic resonance imaging (MRI) is able to obtain images of the heart and great vessels with an entire coverage of the cardiovascular system for assessment of anatomy, function and flow. Time-resolved three-dimensional phase-contrast MRI (3D cine PC-MRI or 4D Flow) [28, 12] has been proposed to acquire an anatomical image and velocity encoded images in three orthogonal directions. 4D Flow has the capacity to measure non-invasively the 3D-spatial and temporal evolution of complex flow patterns, allowing the quantification of different hemodynamic parameters [29]. In particular, 4D Flow allows to infer pressure maps using the Navier–Stokes equations along the thoracic aorta.

In order to obtain those maps, the classical method is solving a Pressure Poisson Estimator (PPE) by taking the divergence of the Navier–Stokes equations and inserting the velocity measurements in the right-hand-side [15, 25]. More recently, several additional methods have been introduced, a comprehensive review can be found in [4]. In particular, the Stokes Estimator (STE) [43] computes 3D pressure maps using a Stokes equation based on the physical pressure and an auxiliary, non-physical velocity field.

In addition to PPE and STE, less computationally expensive methods exist, like the Work Energy-derived Relative Pressure (WERP) method [11] based on an integral energy balance of the Navier–Stokes equation, the integral momentum relative pressure estimator (IMRP) [4] based on integral linear momentum conservation, or the virtual WERP (vWERP) method [31] based on a different treatment of the convective term than in the IMRP. Using numerical data, the WERP has shown better accuracy than the PPE, but worse accuracy than the STE and IMRP, while the two latter were shown to have similar accuracy [4]. The WERP also assumes that the studied vessel segment does not have bifurcations. As a consequence, it cannot be used to estimate the pressure difference between the ascending and

the descending aorta due to the presence of the supra-aortic branches. Moreover, WERP, IMRP and vWERP can only deliver mean pressure differences between two planes of the vessel of interest, and they are therefore difficult to apply in cases when pressure spatial variations are present as in post stenotic areas. For all the aforementioned reasons, in this work we consider only the PPE and the STE methods.

Several validation studies were carried out for the PPE method [38, 39, 18]. An in vitro validation study showed a good correlation between PPE and catheter pressure differences ($r = 0.89$, $p < 0.001$) in the simple setting of an elastic straight tube phantom [38]. The PPE method was further assessed in 13 patients with moderate AoCo in [39], where instantaneous peak pressure differences from 4D Flow were found to be slightly underestimated on average in comparison to the catheterization data, with a bias of 1.5 mmHg and a variability of ± 4.6 mmHg (two standard deviations). Also in [18], PPE pressure differences showed good agreement with catheter measurements in AoCo patients in cases with sufficient spatial image resolution (at least 5 voxels/diameter). However, systematic underestimation of the pressure difference was found for lower resolutions (3.4 ± 0.64 voxels/diameter).

To the best of the authors' knowledge, no validation studies have been reported for the STE method using experimental or patients' 4D Flow and catheterization data. The aim of this work is therefore to fill this gap and study the effects of the MR image resolution and aortic segmentation, cardiac output and severity of the aortic coarctation on the accuracy of both PPE and STE methods from 4D Flow and catheterization data. This is achieved by using data from a realistic MRI compatible aortic coarctation phantom that the authors have designed and studied [45]. We have also included the comparison of these methodologies in 2 patients. The present study is the first reported validation of the STE method using measured data.

2 Theory

2.1 Problem statement

Maps of relative pressure can be computed directly from the velocity measurements by evaluating the linear momentum conservation equation of the incompressible Navier–Stokes model, i.e.

$$-\nabla p = \rho \frac{\partial \vec{u}}{\partial t} + \rho(\vec{u} \cdot \nabla)\vec{u} - \mu \Delta \vec{u} \quad (1)$$

where ρ is the density of the fluid and μ its dynamic viscosity, $\vec{u} : \Omega \rightarrow \mathbb{R}^3$ denotes the velocity vector field and $p : \Omega \rightarrow \mathbb{R}$ is the pressure field. Ω represents the computational domain obtained from segmenting the 4D Flow images. By inserting the 4D Flow velocity data into \vec{u} , the pressure gradient can be recovered by applying numerical methods. In this work we use the Pressure Poisson Estimator (PPE) approach [15, 14, 25] and the Stokes Estimator method (STE) [43, 9], which will be described in this section.

Discretizing Equation (1) in time, here with the first order backward difference formula, gives the following expression for the pressure gradient:

$$-\nabla p^k = \rho \frac{\vec{u}^k - \vec{u}^{k-1}}{\Delta t} + \rho(\vec{u}^k \cdot \nabla)\vec{u}^k - \mu\Delta\vec{u}^k. \quad (2)$$

The indices $1 \leq k \leq N$ denote the time snapshot of the measurements and Δt the temporal offset between two consecutive measurements or cardiac phases, with time stamps $t_k = k\Delta t$. For the first step, $k = 1$, a forward difference has to be used instead since no previous measurements are available. Evaluating the right hand side of Equation (2) for spatially undersampled and noisy velocity measurements \vec{u}_m ,

$$R^k := \rho \frac{\vec{u}_m^k - \vec{u}_m^{k-1}}{\Delta t} + \rho(\vec{u}_m^k \cdot \nabla)\vec{u}_m^k - \mu\Delta\vec{u}_m^k. \quad (3)$$

yields a pressure estimate from its approximate gradient $\nabla\hat{p}^k \approx \nabla p^k$, given by

$$-\nabla\hat{p}^k = R^k. \quad (4)$$

Higher order time schemes, while more accurate in theory for small time steps, are not beneficial in the present context due to the coarse time sampling of the measured velocities. Note that in previous works, for instance in [4, 31] a second-order mid-point scheme was used. However, this leads to stronger underestimations of the pressure differences. This can be explained from the nature of time under-sampling in MRI, namely that u_m^k is reconstructed by assuming the flow velocity as constant within the interval $[t^k - \Delta t/2, t^k + \Delta t/2]$ rather than being an instantaneous measurement at t^k [29].

It is important to remark that in all methods derived from the Navier–Stokes equations, e.g., Bernoulli-based, PPE, STE, and in CFD simulations, at any instant of time, the pressure is uniquely defined up to a constant (with respect to the spatial coordinates). Therefore, only instantaneous pressure differences between different locations can be compared at different times. Catheterization or sphygmomanometer pressure measurements are taken relative to the atmospheric pressure. Hence, the pressures are calibrated with respect to a global reference and pressure values can be compared at different times and among patients. A common measure in the clinical practice are the so-called peak-to-peak pressure differences, which compares the largest pressure difference registered between two locations at any time during the cardiac cycle, thus taking into account time shifts due to the vessel elasticity. Peak-to-peak pressure differences can only be determined by means of catheterization or with the models described above when calibrated with catheterization data, which however violates the non-invasiveness of the estimation methods. For this reason, the present work focuses on instantaneous pressure differences instead of peak-to-peak values.

Based on Equation (4), the Pressure Poisson Estimator (PPE) and the Stokes Estimator (STE) method will be described next.

2.2 Pressure Poisson Estimator (PPE)

Assuming sufficient regularity (i.e., assuming that all required derivatives exist), a Poisson equation for the pressure estimation can be obtained by taking the divergence of the time-

discrete Navier–Stokes equation (2),

$$-\Delta \hat{p}^k = \nabla \cdot R^k. \quad (5)$$

Solving Equation (5) requires boundary conditions (BCs) on the boundary $\partial\Omega$ of the computational domain. A priori, no physical BCs for the pressure are known. An artificial Neumann BC can be obtained by projection of Equation (4), restricted to $\partial\Omega$, to the outward unit normal vector on the wall, \vec{n} ,

$$\vec{n} \cdot \nabla \hat{p}^k = \vec{n} \cdot R^k. \quad (6)$$

Equation (5) with BCs (6) can be discretized in space and solved with the finite element, finite volume or finite difference methods. Independently on the spatial discretization, in order to ensure that the resulting algebraic problem is uniquely solvable, an option is to fix $\hat{p}^k = 0$ at one point via a Dirichlet boundary condition. This, indeed, does not change the pressure differences between two points in space.

2.3 Stokes Estimator (STE)

The Stokes Estimator introduces a divergence-free auxiliary function \vec{w} with $\vec{w} = \vec{0}$ on $\partial\Omega$. The Laplacian of \vec{w} is subtracted from Equation (4) as a regularization term (with unitary viscosity here for simplicity) and we obtain

$$\begin{aligned} -\Delta \vec{w} - \nabla \hat{p}^k &= R^k && \text{in } \Omega \\ \nabla \cdot \vec{w} &= 0 && \text{in } \Omega \\ \vec{w} &= \vec{0} && \text{on } \partial\Omega. \end{aligned} \quad (7)$$

The auxiliary function \vec{w} holds no physical interest, and it is expected to be negligible compared to the pressure term as long as the right-hand-side R^k is the gradient of a scalar (irrotational). The advantages of the STE with respect to the PPE method are (1) that no artificial BCs for the pressure are necessary and (2) it has lower regularity requirements, since no additional derivatives are applied on the measurements R^k . In fact, in contrast to the PPE method, the STE method searches the pressure in the natural energy space of the pressure in the original Navier–Stokes equations [44]. As for the PPE method, the pressure constant has to be fixed for ensuring solvability of the algebraic problem.

A variation of the STE method was presented in [4], where the convective term was written in ‘energy-conserving’ form, $(\vec{u} \cdot \nabla) \vec{u} + \frac{1}{2}(\nabla \cdot \vec{u}) \vec{u}$, and improved results were obtained compared to the standard method. A third way of formulating the convection term is the divergence form $\nabla \cdot (\vec{u} \otimes \vec{u})$. In a preliminary study, the standard method, Eq. (3) (results not shown here), consistently delivered more accurate results than the other variants. Hence only results obtained using the standard STE formulation will be reported here.

3 Methods

3.1 Aortic Phantom Study

3.1.1 Phantom setup

The experimental setup of the aortic phantom study is described in detail in [45] and [32]. The phantom represents the thoracic aortic circulation with a closed circuit, consisting in a MR-compatible pulsatile unit pump with a control unit (CardioFlow 5000 MR, Shelley Medical Imaging Technologies, London, Canada) and a realistic aortic model built with flexible silicone (T-S-N 005, Elastrat, Geneva, Switzerland). The control unit was configured to simulate two aortic flow conditions and was calibrated with average data of ten healthy volunteers. The MR-compatible pulsatile pump unit has a maximum output peak flow of 300 mL/s, therefore, the output peak flow programmed in the pump unit was scaled for rest condition with a peak flow of 200 mL/s and for stress conditions with a peak flow of 300 mL/s. With these conditions programmed in the pump, the peak flow measured in the ascending aorta was 270 mL/s at rest and 352 mL/s at stress conditions. Additionally, nonreturn valves were employed in order to avoid negative pump pressures during diastole. Shutoff valves in the DAo and supra-aortic vessels were used for reproducing the peripheral resistance of the circulatory system and to regulate the flow distribution between the different vessels. A compliance chamber was installed after the DAo in order to simulate arterial compliance, to obtain physiologic diastolic pressures and physiologic pressure waveforms.

Different degrees of aortic coarctation were placed in the descending aorta just after the left subclavian artery (at the isthmus level). Aortic coarctations were built with Technyl with an effective orifice of 13, 11 and 9 mm and a length of 10 mm, leading to degrees of stenosis of 40 %, 50 % and 60 % with respect to the native DAo distal to the AoCo. The liquid used in the system consisted of a homemade volume-mixing blood mimicking fluid with 60 % distilled water and 40 % glycerol (Orica Chemicals, Watkins, CO), with a density of 1.119 g/cm^3 , viscosity of $4.83 \times 10^{-3} \text{ Pas}$ [5, 23], and a T1 value of 900 ms, which are representative values for human blood. The density and viscosity values of the mixture were confirmed using an empirical formula reported by [10] with an ambient temperature of 22 °C.

3.1.2 Catheterization

The phantom was equipped with a catheterization unit to measure invasively and simultaneously the pressure gradient across the coarctation. For this purpose, two catheters (5 French, Soft-Vu, AngioDynamics, Latham, NY) of side-hole type with transducers (AngioDynamics) were placed in the AAo and 2 cm after the AoCo and were connected to a patient monitor (Contec Medical Systems, Hebei, China). The pressure catheters were zeroed at the same height of the phantom.

Pressure information from the two catheters was recorded simultaneously during 1 minute in the AoCo phantoms (40 %, 50 % and 60 % degrees of stenosis) at rest (75 bpm) and at stress conditions (136 bpm), using the commercial software Central Monitor System V3.0

(Contec Medical System). The pressure difference is obtained by subtracting the averages of both signals over the cardiac cycles.

A lower bound of the catheter errors can be estimated from the standard deviation of the pressure signals at fixed times across the cardiac cycles. This value lies mainly within 1.5 mmHg for both measurement positions. The standard deviation of the pressure difference is then $\sqrt{2} \cdot 1.5 \text{ mmHg} = 2.12 \text{ mmHg}$, leading to a 95 % confidence interval of around 5 mmHg.

3.1.3 4D Flow data acquisition

Phantom data were acquired in a 1.5 T MRI system (Achieva, Philips, The Netherlands) using a 4-channel body coil and retrospective cardiac gating. The control unit of the pulsatile pump generated a trigger signal to synchronize the MR data acquisition. In order to provide static tissue for phase correction algorithms used in PC-MRI, 6 liters of 1 % agar were placed around the aortic phantom at least 6 hours before scanning.

4D Flow images were acquired with an isotropic voxel size of 0.9 mm for all phantoms (AoCo with 40 %, 50 % and 60 % degrees of stenosis) under rest and stress conditions. In order to study the effect of image resolution of the pressure gradient estimation procedure, different synthetic low resolution data (1.4 and 2.0 mm isotropic voxel) were generated from the original image (0.9 mm isotropic voxel) using linear interpolation. The acquisition parameters are summarized in Table 1 (see column “in-vitro experiments”).

3.2 Patient study: 4D-Flow MRI and catheterization

In addition to the phantom study, we include two subjects with aortic coarctation (Subject 1: 12 years, weight 47 kg, height 151 cm; Subject 2: 35 years, weight 63 kg, height 205 cm). Subject 1 presented a native aortic coarctation and mild aortic valve stenosis, mild left ventricular hypertrophy and systemic hypertension at rest. Subject 2 presented a repaired AoCo using a subclavian flap, situs solitus, there was a very mild narrowing at the level of the transverse arch, close to the isthmus and a mild dilatation in the proximal descending aorta. Angiographic contrast agent enhanced images of the patients’ aortas with anatomical information and 4D Flow streamlines are displayed in Figure 8(a).

The clinical patient data were acquired in a combined MRI/Catheter interventional suite (XMR, see [42] for a more detailed description), equipped with a 1.5T Achieva MR scanner and a BT Pulsera cardiac radiography unit (Philips, Best, Netherlands) [37, 33]. Patients had general anesthesia according to institutional protocol. Two femoral artery vascular accesses by percutaneous puncture were performed. A heparin bolus of 50 IU/Kg was given with activated clotting time monitoring once vascular access was obtained. A MRI compatible multi-purpose catheter was advanced under fluoroscopic guidance from the right femoral artery to the ascending aorta just above the aortic sinus for continuous hemodynamic pressure monitoring. A second multi-purpose catheter in the left femoral artery was advanced to the abdominal aorta at the level of the diaphragm. The catheter positions are visually determined during the fluoroscopy procedure by the interventionist. We used these positions in the 4D flow based pressure computation as shown in Figure 8. The floating table

Table 1: MR acquisition parameters

	in-vitro experiments	in-vivo experiments
FOV (mm)	$200 \times 200 \times 114$	$270 \times 270 \times 125$
Matrix size	$224 \times 224 \times 127$	$144 \times 144 \times 50$
Recon. voxel (mm)	$0.9 \times 0.9 \times 0.9$	$1.9 \times 1.9 \times 2.5$
TFE factor	rest: 2, stress: 1	rest: 2
Cardiac phases	25	28
Time resolution (ms)	AoCo: rest: 32, stress: 18 Normal: rest: 35, stress: 19	rest: 26
VENC (cm/s)	AoCo: rest: 160–400, stress: 250–500 Normal: rest: 150, stress: 150	rest: 300
TE/TR (ms)	3.7/6.4	2.4/3.8
Flip angle (deg)	6.5	5
Scan time (min)	18–22	19

was then moved to transfer the patient to the MRI scan to acquire the 4D flow MRI data. Following the acquisition of the MR data the patient was transferred back to the catheter table. Catheter pullbacks were performed using a biplane system (Siemens Axiom-Artis d-TA, Siemens, Germany) for evaluating the pressure distribution along the aorta. X-rays images were acquired with a frame rate of 15 images per second.

The data was acquired at St. Thomas’ Hospital, London, UK. The local research ethics committee approved this retrospective study and informed consent was obtained from all patients.

The acquisition parameters for the in vivo study are summarized in Table 1 (see column “in vivo experiments”). Moreover, the cardiac output obtained from the 4D flow data for subjects 1 and 2 are 3.27 L/min and 6.49 L/min, respectively.

3.3 Segmentation and mesh generation

The 4D Flow data sets were processed using an in-house MATLAB library (The MathWorks, Natick, MA), similarly to previous studies [41, 40]. The library contains a homemade segmentation toolbox, which consists in (a) a contrast adjustment of the images to increase the intensities in the vessel of interest, prior to (b) performing a 3D threshold and 3D labeling of the different regions of interest in the images. If the user agrees with the selected thresholding level, the next step (c) is the iterative manual disconnection of different objects inside the image. 3D labeling at this step is used to verify that the disconnection was performed properly.

For patients, we perform the segmentation over the angiographic image as described in [6], which is the time average of the anatomic images multiplied by the magnitude of the

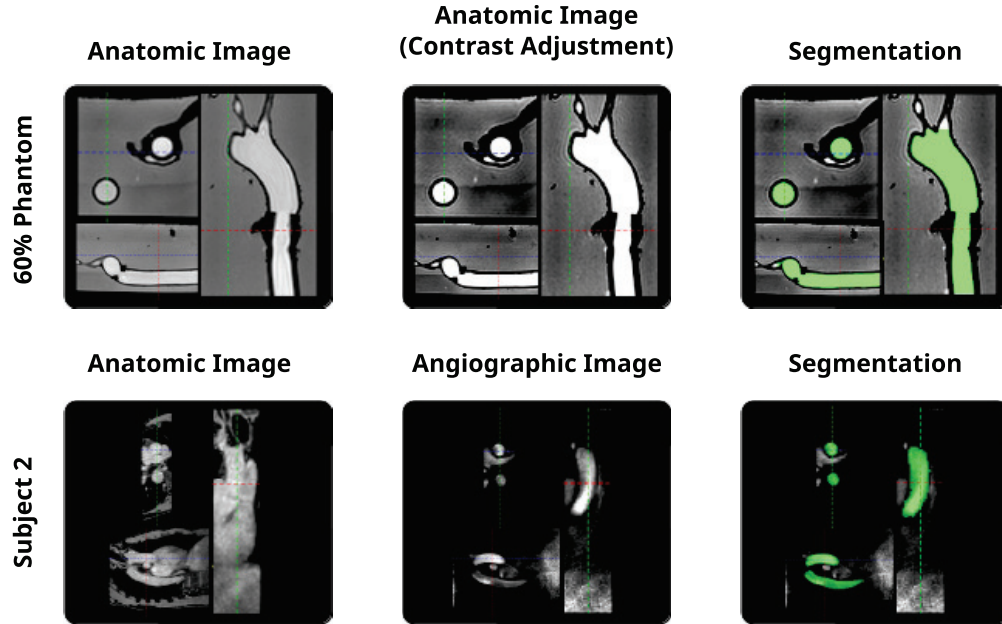


Figure 1: Segmentation procedure. Phantom data (first row, 60% degree of stenosis example): (a) anatomic images (left column) are enhanced by contrast adjustment (middle column), before (b) applying a 3D threshold and region labeling and (c) iteratively performing manual disconnection of different objects present in the image for each slice, to yield the final segmentation (right column). Patient data (second row): instead of a contrast adjusted anatomic image, step (a) produces an angiographic image, steps (b) and (c) as for phantom data.

velocities images. For the phantom data, we perform the segmentation over the average time of the anatomic images, because, different to patient data, here we can obtain good contrast between the lumen of the vessel and the agar-agar used in the phantom reservoir.

The procedure is illustrated in Figure 1.

By segmenting the 4D flow images rather than using the known CAD geometry, the true state of the phantom during the experiment is considered, i.e., deformation due to fluid pressure and installation in the test rig. Moreover, due to the excellent contrast between the fluid and the silicone (see Figure 2(a)), the anatomical image gives an accurate measure of the geometry and can be segmented using a simple threshold and 3D labeling.

From the final segmented image, we generated a structured tetrahedral mesh (Figure 2(b)) such that its vertices matched the centers of the image voxels. The velocity vectors attributed to each voxel of the 4D flow images were transferred to the corresponding mesh vertices (Figure 2(c)).

The last step in the toolchain consists in the pressure map reconstruction (Figure 2(d)), described in the next section.

In order to study the effect of different segmentations on the pressure difference estimates, additional segmentations were created for the phantom velocity images at 0.9 mm voxel size.

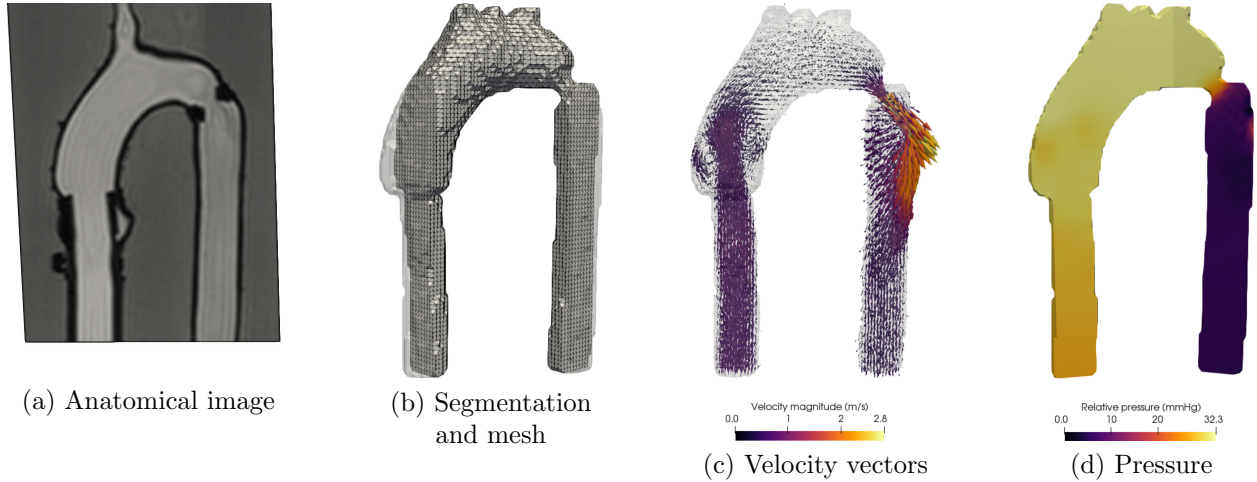


Figure 2: Pressure recovery toolchain. (a) 2D section from the anatomic image of 4D Flow, (b) structured tetrahedral mesh (grey, cropped) from segmentation (transparent) of the anatomical image, (c) representation of 4D Flow velocity vectors on mesh, (d) pressure maps from velocity data (cuts through centers of AAO and DAAo). Example data of the 60% AoCo phantom at rest, at time of peak systole.

A reference segmentation was modified by adding or subtracting one voxel at the boundary, thus extending or decreasing the lumen cross-section.

For the patient data, only the original segmentations obtained with the procedure described above were used, since the large voxel size of 2 mm with respect to the aortic diameter did not allow eliminating boundary voxels in on of the patients.

3.4 Pressure maps computation

Pressure maps are computed from all 4D Flow data sets with the PPE and STE methods. The pressure differences, to be compared with the corresponding catheter values, are defined as differences of the pressure averages over two spheres with a radius of 4 mm at locations proximally and distally to the AoCo (e.g., the colored spheres in Figures 3 and 8(a) (right column)). Averaging over several voxels renders the pressure estimate more robust to local perturbations, e.g., induced by noise in the 4D flow data.

The corresponding partial differential equations of the PPE and STE methods are discretized with the finite element method (FEM). Velocity measurements are assumed to be piece-wise linear (\mathbb{P}^1) finite element functions on the tetrahedral meshes described in the previous section. Linear \mathbb{P}^1 elements are also used to discretize the PPE and the STE systems, Equations (5) and (7). In the latter case, standard pressure stabilization (Brezzi–Pitkaranta) is employed to ensure the solvability of the saddlepoint problem, avoiding the need of higher order elements. A sample pressure map computation is shown in Figure 2(d), as result of the last step of the pressure recovery toolchain, described in the previous section and illustrated

in Figures 2(a)–(d). The code was implemented using the python/C++ FEM library FEniCS [1] and linear algebra solvers from the scientific computation library PETSc [3]. With the FEM discretization as indicated, the resulting algebraic linear system of the STE problem is four times larger than that of the PPE method, resulting in higher memory requirements and computational times. Direct solvers are efficient for solving the linear systems, taking advantage of re-using the LU factorization of the system matrix at the first time-step for all subsequent steps.

The results presented in this article were computed on a standard desktop computer with 32 GB RAM and an Intel i7-4790K CPU.

4 Results

4.1 Phantom study

The streamlines of the 4D Flow velocity field and the pressure signals measured by catheterization in the indicated locations in the AAo and DAo are illustrated in Figure 3 for the 60 % degree of stenosis AoCo phantom at peak systole. In addition, the instantaneous pressure difference resulting from subtracting both signals is plotted. For the 60 % phantom, the flow in the downstream catheterization location was in fact not entirely parallel with respect to the vessel orientation, thus possibly inducing a dynamic pressure contribution in the side-hole catheter. This contribution was estimated < 2.5 mmHg for the 60 % AoCo at rest (of the order of the catheter uncertainty) leading to a slight overestimation by the true pressure difference, and negligible in the other cases.

Figure 4 compares the instantaneous peak pressure differences obtained with the PPE and the STE methods from 4D Flow with catheterization data for all investigated phantoms. The figure shows the data obtained with the three image resolutions, 0.9 mm, 1.4 mm and 2.0 mm and using the three segmentations, denoted V+0 (initial segmentation), V−1 (outermost layer of voxels eliminated along the boundary) and V+1 (1 layer of voxels added at the boundary).

Consider first the results obtained on the V+0 segmentation. The results show an overall good agreement between the STE peak pressure differences and the catheterization data. The STE underestimates the highest measured pressure difference (catheter pressure difference of 46 mmHg with the 60 % AoCo phantom under stress conditions). Another underestimation is visible at 12 mmHg in all plots, which was obtained for the 40 % phantom at rest. The results appear to be robust to the image resolution. A strong dependence on the segmentation exists particularly for pressure differences above 30 mmHg and is more pronounced for large voxel sizes. The PPE method, in comparison, leads to a stronger underestimation than the STE method for pressure differences ≥ 20 mmHg. The PPE results are more sensitive to the image resolution.

In the presence of large pressure differences, both the PPE method and the STE method generally benefit from the narrowed segmentation (denoted V−1 in the figure). In the range of moderate pressure differences (e.g., 10–20 mmHg), the most accurate results with the STE

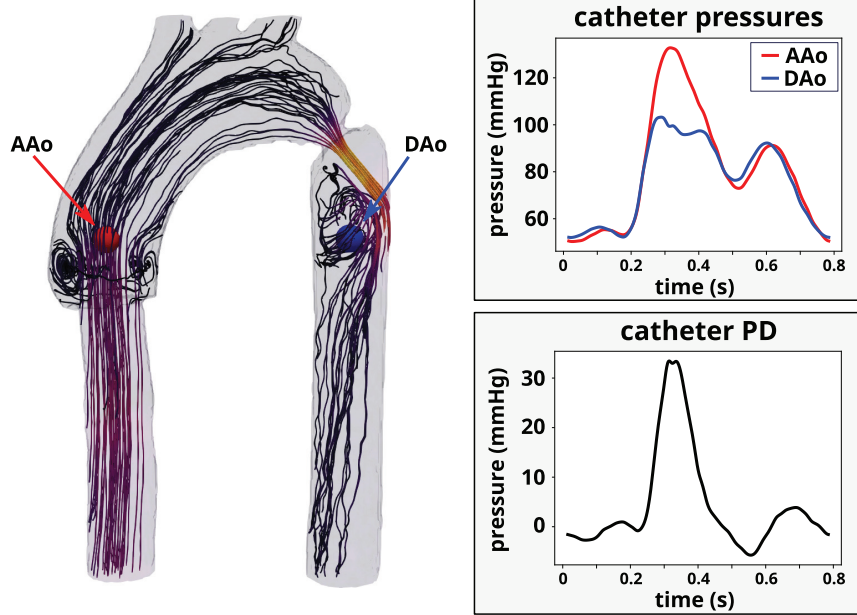


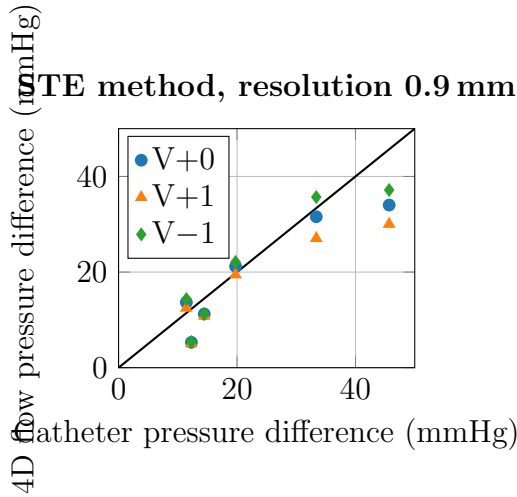
Figure 3: 4D Flow MRI velocity streamlines (left), catheterization pressure signals, measured at AAo (red) and DAo (blue) locations (upper right), and pressure difference (PD) resulting from subtracting both pressure signals. Example of 60% AoCo at rest at time of peak systole.

method were obtained on the reference segmentation, while the $V-1$ segmentation led to a slight overestimation. The accuracy of the PPE method however was improved throughout the entire range of pressure differences. This is likely because of an increased sensitivity to boundary issues such as partial volume effects and low VNR (velocity-to-noise ratio) due to the artificial pressure boundary conditions. Choosing the segmentation too large resulted in underestimating the pressure differences ($V+1$ values in Figure 4).

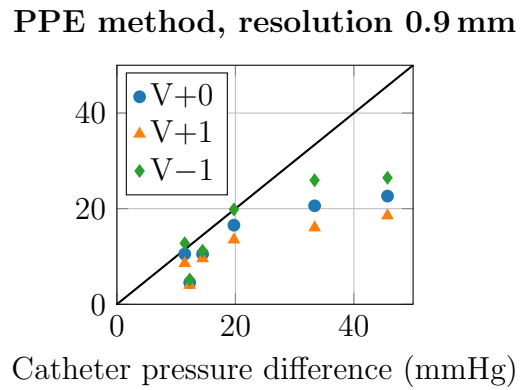
The root-mean-square errors (RMSE) of the pressure difference estimates obtained with the PPE and the STE methods with respect to catheterization data are compared for the three segmentations, $V+0$, $V-1$ and $V+1$ in Table 2. The data is shown for the time of peak systole using 4D Flow images with a resolution of 0.9 mm. For both methods, the errors are

Table 2: Root-mean-square error (RMSE) of PPE and STE pressure difference estimates compared to catheterization measurements for all severities (40%, 50% and 60% AoCo under rest and stress conditions) at peak systole with the initial segmentation $V+0$, the reduced lumen diameter segmentation $V-1$ and the dilated lumen segmentation ($V+1$). Resolution of 4D Flow MRI data: 0.9 mm.

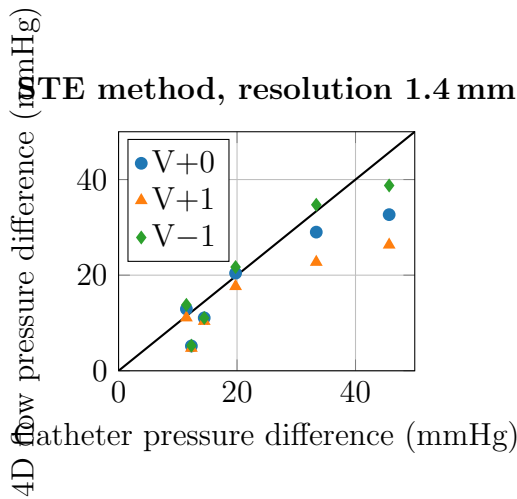
method	Root-mean-square error (RMSE)		
	segmentation $V+0$	segmentation $V-1$	segmentation $V+1$
PPE	11.41 mmHg	9.01 mmHg	14.01 mmHg
STE	5.85 mmHg	5.00 mmHg	7.65 mmHg



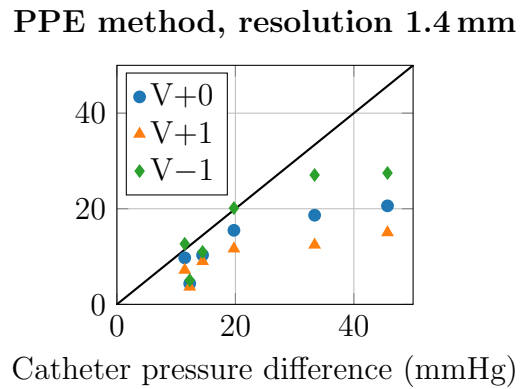
(a)



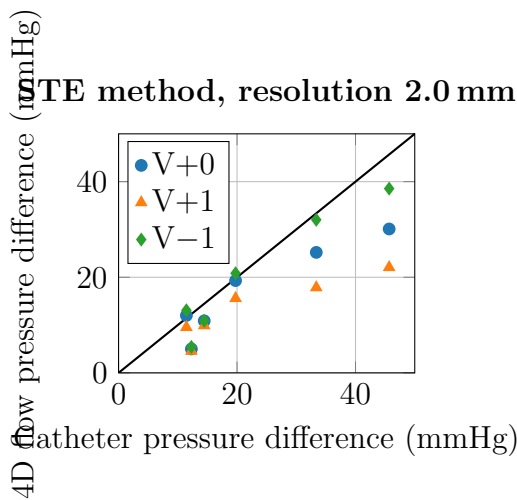
(b)



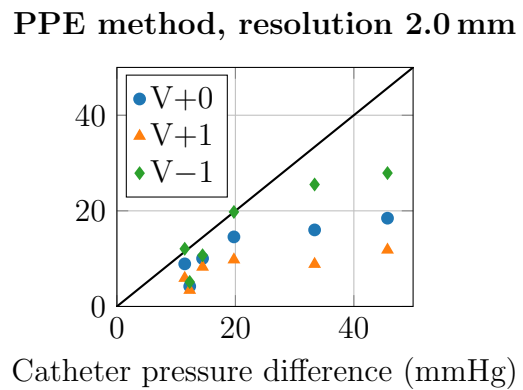
(c)



(d)



(e)



(f)

Figure 4: Comparison of 4D Flow peak pressure differences obtained with the STE (left column) and the PPE (right column) methods with respect to catheterization, for all in-vitro severities (AoCo with degrees of stenosis of 40 %, 50 % and 60 % at rest and stress). Figs. (a) and (b) show results obtained using an image resolution of 0.9 mm, (c) and (d) a resolution of 1.4 mm, and (e) and (f) a resolution of 2.0 mm. V+0 refers to a reference segmentation.

smallest on the reduced segmentation $V-1$ and largest on the extended segmentation $V+1$, with the reference segmentation $V+0$ ranking in between. The RMSE of the STE method are lower than the PPE errors by approximately 50%, implying an important improvement of overall accuracy with STE. In addition, the PPE method appears to be more sensitive to the lumen segmentation, as the RMSE varies more strongly depending on the segmentation.

Time profiles of the pressure differences obtained with the $V-1$ segmentation are shown in Figures 5–7. Each figure contains the results of the PPE and the STE methods for 4D Flow resolutions of 0.9 mm (acquired) and 1.4 mm, 2.0 mm (subsampling from 0.9 mm) under rest and stress conditions and the pressure difference from catheter measurements.

The results of the 40% AoCo phantom study are displayed in Figure 5. While showing qualitatively a correct behavior, the amplitude of the oscillation is generally underestimated by 3 to 7 mmHg with both methods under rest conditions. The effect of the image resolution is hardly noticeable. Both methods yield very similar results for the 40% degree AoCo. Under stress conditions, the peak pressure difference is recovered with a good accuracy. There is a negative pressure difference peak that was not correctly recovered by any of both methods. It has to be noted that in the particular case of the 40% AoCo phantom, artifacts appeared in the velocity measurements, most likely connected to issues with the experimental setup, like bubbles. The 40% AoCo phantom configuration was repeatedly scanned at different resolutions (results not reported) and the corresponding estimated pressure differences showed similar characteristics in all cases. The difference in the width of the systolic peak interval between the 4D Flow data and the catheter data is also likely to be caused by such issues with the experimental setup.

In the case of the 50% AoCo phantom, the PPE method exhibits a very good quantitative agreement with the catheter results under rest conditions during the complete heart cycle (Figure 6(b)). In comparison, the STE method overestimates the peak pressure difference. The STE result is improved by using the standard segmentation instead of the narrowed segmentation. Under stress conditions, the width of the pressure differences maxima was overestimated with both the STE and the PPE methods.

Results from the 60% AoCo phantom under rest conditions showed an excellent agreement between the catheter data and the pressure difference computed with the STE method (Figure 7, panel (a)). The PPE method strongly underestimates the pressure difference under equal conditions (panel (b)). The discrepancy between the pressure difference reconstruction and catheter measurements increases for stress conditions, the STE method still showing more accurate results than the PPE method. Both methods are very robust with respect to the image resolution. Using the narrowed segmentation, the results of the stress case are slightly improved by the lower resolutions. With low resolution data, effectively more boundary data is discarded by deleting the outermost voxel layer. This indicates that the errors introduced by considering boundary data predominate the effect of image resolution in this scenario. In contrast, in Figure 4 the $V+0$ pressure differences at 46 mmHg decrease with lower image resolutions.

As a consequence of the larger linear system arising from the discretization of the STE equations by a factor of 4 compared to the PPE method, the STE method requires longer

computational times and has a higher demand in RAM. For example, the 40% AoCo phantom with 2 mm voxel size takes approximately 7.4 s to compute with the PPE method while the STE method takes twice as long, 14.9 s, to complete with the direct solver MUMPS [2] on an Intel i7-4790K CPU. With a higher resolution of 0.9 mm voxel size, the PPE method computed all pressure maps in 35 s. For STE the computational time in this case is increased to 247 s.

4.2 Patient data

Pressure differences obtained by catheterization and from 4D Flow are shown in Figure 8(c) and (d) for both patients. The locations where the pressure difference is evaluated is indicated by the green spheres in Figure 8(a) (right column). The pressure difference computed with the STE method for subject 1 shows excellent agreement with the catheter data during systole, underestimating the local extrema after $t = 0.4$ s. While similar qualitative agreement was found with the PPE method, it significantly underestimates the pressure difference during systole.

Subject 2 exhibits excellent qualitative and quantitative agreement between catheter data and numerical pressure difference reconstruction. However, the pressure difference peak observed by catheterization is too steep to be captured by the time resolution of the 4D Flow protocol. The resulting maximum value lies below the catheter value, possibly because no velocity image was recorded matching exactly with the maximum pressure difference.

Note that the lengths of the cardiac cycles differ significantly between catheterization and MRI scans of both patients. This indicates a change in the heart rate and hence, the hemodynamics in the cardiovascular system, and can explain the differences between 4D Flow and catheter pressure differences.

Reducing the diameter of the segmentation by one voxel was not possible in one of the patients due to the large voxel size with respect to the diameter. The original segmentations were thus not modified.

5 Discussion

This study compared two relative pressure reconstruction methods, STE and PPE, in terms of accuracy and sensitivity with respect to image resolution, segmentation, AoCo severity and cardiac load (rest and stress).

The main finding of this study is that the STE method applied to measured data is more accurate than the classical PPE method at large pressure differences (>20 mmHg). The difference between the methods is less pronounced for small to moderate pressure gradients.

The superiority of the STE method in most cases can be explained by the fact that it searches the pressure in its natural space, allowing for stronger spatial variations in the pressure, while the PPE method essentially computes smoothed pressure fields due to using higher derivatives in the mathematical formulation. This issue becomes more evident for higher Reynold's numbers, where the pressure gradient is mainly convection dominated.

Furthermore, the STE method avoids unphysical pressure boundary conditions, required by the PPE method, which can contaminate the solution with noisy boundary data (very low VNR, partial volume effects).

The PPE method showed overall a higher sensitivity to data perturbations, i.e., to image resolution and segmentation. Both the STE and the PPE methods proved most sensitive to the image resolution and the segmentation in the most severe cases of 50 % and 60 % AoCo during systole. Especially the PPE results were greatly improved by eliminating the outermost layer of voxels from the segmentation, leading to a more accurate match with the catheter data than STE in the 50 % AoCo phantom. However, the STE method gave excellent results in this case using the standard segmentation. A reduction of the segmentation was used before in [18] and also led to an improved accuracy of the PPE method. The accuracy improvement can be explained by the reduction of partial volume effects and eliminating low VNR data near the boundaries. The PPE method is likely to be more sensitive to the boundary data than the STE method due to the artificial pressure boundary conditions used in the PPE. The issues of boundary data, possible remedies and the effect of somewhat arbitrarily reducing the diameter of the vessel geometry deserve a more in-depth analysis in future studies.

Our results on the standard segmentation (V+0) are consistent with [34, 18], who also demonstrated that the pressure profile is degraded when the spatial resolution is decreased. In [18], minimal resolution requirements were determined for the PPE, namely 5 voxels/diameter. In our study, when the narrowed segmentation was used (V−1, between 2 and 12 voxels/diameter for the AoCo phantoms), the results were almost insensitive to the image resolution. It is possible that the benefit of removing problematic boundary data at low resolutions, apparently increasing under low resolutions, balances with the detriment of a decreased image resolution in the interior.

An advantage of the STE method is that it avoids unphysical boundary conditions. However, using standard discretization methods, parts of the term R^k in Equation (7) can contribute to the auxiliary function w —not always negligible in practice—instead of the pressure gradient. This occurs principally where large gradients are present in the velocity field, for instance in the coarctation near the arterial walls, and can result in stronger underestimations of the relative pressure. We hypothesize that, by choosing a more narrow segmentation with the arterial wall located inside the flow, the homogeneous Dirichlet boundary condition for the auxiliary velocity in the STE on the smaller domain results in a smaller auxiliary velocity everywhere and therefore in increased pressure gradient estimates with respect to the full geometry for severe AoCo. Pressure-robust FEM could counteract this issue [27] and generally improve the accuracy of the STE method.

Dilated segmentations (V+1) add no-flow voxels with very small VNR, hence introducing spurious information into the estimation problem. The pressure gradient computed with any method is required to accommodate to the unphysical conditions.

For severe conditions of AoCo, i.e., in the presence of high velocity jets and high Reynolds numbers, the STE method was clearly superior to the PPE method. In such severe cases of AoCo, turbulence can develop [26, 13] and involves dynamics at scales smaller than the

spatial and/or temporal image resolution. Such effects are not accounted for by the models studied here, and are likely to reduce the precision especially in the 60% phantom under stress conditions. Furthermore, higher velocities require higher VENC values (500 cm/s for the 60% phantom at stress) resulting in lower VNR, possibly affecting the estimation. Our study did not include sensitivity to noise. However, we can consider the results present here as a “worst case scenario” in terms of noise due to the small voxel size of 0.9 mm, hence involving a much worse VNR than what can be expected for typical voxel size in patients (i.e., around 2 mm). This issue could be alleviated by using the dual-VENC techniques [35, 19, 7, 8], allowing for lower VENC-values (hence lower noise), but at increased scan times.

The STE and the PPE pressure reconstruction methods were also applied to real patient data. For one of the patients, the STE method showed a great improvement over the PPE method. Both methods showed satisfactory results for the second patient. From the findings in the phantom experiments, the differences between PPE and STE in patient one is most likely due to strong convective effects.

One limitation of the study was the lack of availability of real low resolution MRI data for all scenarios, hence requiring synthetic subsampling of the high resolution data. Another aspect to consider is the approach used for assessing the sensitivity to the segmentations, i.e. automatic instead of manual. We use this approach because it was the most appropriate in the phantom data, since as we show in Figure 1 the contrast in the anatomic image of the phantom has a good quality with high SNR. This easily allows a three-dimensional segmentation based on thresholding and labeling. Therefore, if different users applied this process the difference in the results would likely be negligible. Thus, in order to ensure different segmentations in these controlled experiments, we opted for the voxel increment or decrement at the vessel boundary. But in the patient data we could have expected larger deviations when among users when manual segmentation is performed.

In addition, the comparison of catheter data with MRI scans is limited by the following observations. The locations where the catheter recorded the pressure during catheterization are only known approximately. Fluctuations in the flow can also perturb the catheter position. A mismatch of the catheter positions with the locations selected for evaluating the computed pressure gradient can introduce additional errors. Finally, representing an invasive technique, it is possible that the presence of the catheter in the vessel disturbs and alters the aortic flow during catheterization, while the 4D Flow data was acquired immediately after without the catheters. In the patient study it was seen that the heart rate changed significantly between catheterization and the MRI scan, hence possibly also affecting the outcome of this comparison.

The Navier–Stokes equations (1) are written in terms of the instantaneous velocity and pressure and take into account turbulence effects over the full range of scales of turbulent motion. However, 4D Flow MRI velocity field measurements are averages in time and space, hence rather corresponding to the results of the Reynolds averaged Navier–Stokes (RANS) equations. RANS describe the ensemble-mean velocity and pressure and including turbulence with an additional term, the Reynolds stress tensor $\rho \text{Cov}[\vec{u}, \vec{u}]$ [36]. While in classical CFD

this term needs to be modeled, [13] showed that it can be reconstructed by extending the 4D Flow measurement protocol and reconstruction. Unfortunately, require 3 additional motion encoded acquisitions. Moreover, measuring and estimating the Reynolds stress using such techniques seems very susceptible to noise, requiring a high amount of ‘signal averages (e.g. five in [20]). Probably for those reasons such sequences have been only reported, to our best knowledge, in experimental phantoms under very controlled situations.

In spite of those limitations, some of the pressure difference estimation methods have been extended for turbulence using the extended measurement protocols. The PPE method including the Reynolds stress was assessed in [22]. The term corresponding to the energy dissipated by the Reynolds stress, also called turbulent production, was introduced as a stand-alone method in [21, 20] and was assessed in numerical and experimental phantoms against catheterization. Then in [30], the *v*WERP was extended with the Reynolds stresses, but also the original WERP method. There, using the same phantom datasets as in [20] it was shown that both *v*WERP and WERP improve their accuracy when including the Reynolds stress. So far, no studies have been conducted extending STE method with turbulence effects, where the choice of the probing locations for the pressure difference could be adapted considering the turbulence pressure map too. Extending the STE method is straightforward as it was done for the previous, just by adding an additional term including the Reynolds stress measurements.

In terms of computational time and memory requirements, the STE method is more expensive than the PPE method, although both methods can be computed on a standard PC within seconds for images at typical clinical spatial resolutions or within few minutes for the experimental high spatial resolution.

In conclusion, in our phantom study, the STE method delivered results that were more accurate and robust with respect to resolution and segmentation than the PPE method, in particular in severe cases of AoCo. For cases of mild AoCo the advantage of the STE method was negligible. By eliminating the outermost layer of voxels of the segmentation, the PPE method could be significantly improved to match the accuracy of the STE method, except for very large pressure gradients.

The data will be made available upon request of the interested parties.

conflict of interest

The authors declare no conflict of interest.

References

- [1] Martin Alnæs, Jan Blechta, Johan Hake, August Johansson, Benjamin Kehlet, Anders Logg, Chris Richardson, Johannes Ring, Marie E. Rognes, and Garth N. Wells. The FEniCS Project Version 1.5. Archive of Numerical Software, 3(100), 2015.

- [2] Patrick R. Amestoy, Iain S. Duff, Jean-Yves L'Excellent, and Jacko Koster. A fully asynchronous multifrontal solver using distributed dynamic scheduling. SIAM Journal on Matrix Analysis and Applications, 23(1):15–41, 2001.
- [3] Satish Balay, Shrirang Abhyankar, Mark F. Adams, Jed Brown, Peter Brune, Kris Buschelman, Lisandro Dalcin, Alp Dener, Victor Eijkhout, William D. Gropp, Dinesh Kaushik, Matthew G. Knepley, Dave A. May, Lois Curfman McInnes, Richard Tran Mills, Todd Munson, Karl Rupp, Patrick Sanan, Barry F. Smith, Stefano Zampini, Hong Zhang, and Hong Zhang. PETSc Users Manual. Technical Report ANL-95/11 - Revision 3.10, Argonne National Laboratory, 2018.
- [4] Cristóbal Bertoglio, Rodolfo Nuñez, Felipe Galarce, David Nordsletten, and Axel Osses. Relative pressure estimation from velocity measurements in blood flows: State-of-the-art and new approaches. IJNMBE, 34(2):e2925, February 2018.
- [5] Jelena Bock, Alex Frydrychowicz, Ramona Lorenz, Daniel Hirtler, Alex J. Barker, Kevin M. Johnson, Raoul Arnold, Hans Burkhardt, Juergen Hennig, and Michael Markl. In vivo noninvasive 4D pressure difference mapping in the human aorta: Phantom comparison and application in healthy volunteers and patients. Magnetic Resonance in Medicine, 66(4):1079–1088, 2011.
- [6] Jelena Bock, Alex Frydrychowicz, Aurélien F. Stalder, Thorsten A. Bley, Hans Burkhardt, Jürgen Hennig, and Michael Markl. 4D phase contrast MRI at 3 T: Effect of standard and blood-pool contrast agents on SNR, PC-MRA, and blood flow visualization. Magnetic Resonance in Medicine: An Official Journal of the International Society for Magnetic Resonance in Medicine, 63(2):330–338, 2010.
- [7] Fraser Callaghan, Rebecca Kozor, Andrew Sherrah, Michael Vallely, David Celermajer, Gemma Figtree, and Stuart Grieve. Use of multi-velocity encoding 4d flow mri to improve quantification of flow patterns in the aorta. Journal of Magnetic Resonance Imaging, 43(2):352–363, 2016.
- [8] Hugo Carrillo, Axel Osses, Sergio Uribe, and Cristóbal Bertoglio. Optimal Dual-VENC (ODV) Unwrapping in Phase-Contrast MRI. IEEE transactions on medical imaging, 2018.
- [9] M. E. Cayco and R. A. Nicolaides. Finite element technique for optimal pressure recovery from stream function formulation of viscous flows. Mathematics of computation, 46(174):371–377, 1986.
- [10] Nian-Sheng Cheng. Formula for the viscosity of a glycerol- water mixture. Industrial & engineering chemistry research, 47(9):3285–3288, 2008.
- [11] Fabrizio Donati, C. Alberto Figueroa, Nicolas P. Smith, Pablo Lamata, and David A. Nordsletten. Non-invasive pressure difference estimation from PC-MRI using the work-energy equation. Medical image analysis, 26(1):159–172, 2015.

- [12] Petter Dyverfeldt, Malenka Bissell, Alex J. Barker, Ann F. Bolger, Carl-Johan Carlhäll, Tino Ebbers, Christopher J. Francios, Alex Frydrychowicz, Julia Geiger, Daniel Giese, Michael D. Hope, Philip J. Kilner, Sebastian Kozerke, Saul Myerson, Stefan Neubauer, Oliver Wieben, and Michael Markl. 4D flow cardiovascular magnetic resonance consensus statement. J Cardiovasc Magn Reson, 17(1), December 2015.
- [13] Petter Dyverfeldt, Andreas Sigfridsson, John-Peder Escobar Kvitting, and Tino Ebbers. Quantification of intravoxel velocity standard deviation and turbulence intensity by generalizing phase-contrast MRI. Magn. Reson. Med., 56(4):850–858, October 2006.
- [14] Tino Ebbers and Gunnar Farnebäck. Improving computation of cardiovascular relative pressure fields from velocity MRI. Journal of Magnetic Resonance Imaging, 30(1):54–61, 2009.
- [15] Tino Ebbers, L. Wigstrom, A. F. Bolger, Bengt Wranne, and Matts Karlsson. Noninvasive measurement of time-varying three-dimensional relative pressure fields within the human heart. Journal of biomechanical engineering, 124(3):288–293, 2002.
- [16] Raimund Erbel, Victor Aboyans, Catherine Boileau, Eduardo Bossone, Roberto Di Bartolomeo, Holger Eggebrecht, Arturo Evangelista, Volkmar Falk, and Herbert Frank. 2014 ESC Guidelines on the diagnosis and treatment of aortic diseases: Document covering acute and chronic aortic diseases of the thoracic and abdominal aorta of the adult. The Task Force for the Diagnosis and Treatment of Aortic Diseases of the European Society of Cardiology (ESC). EHJ, 35(41):2873–2926, 2014.
- [17] Timothy F. Feltes, Emile Bacha, Robert H. Beekman III, John P. Cheatham, Jeffrey A. Feinstein, Antoinette S. Gomes, Ziyad M. Hijazi, Frank F. Ing, Michael De Moor, and W. Robert Morrow. Indications for cardiac catheterization and intervention in pediatric cardiac disease: A scientific statement from the American Heart Association. Circulation, 123(22):2607–2652, 2011.
- [18] Leonid Goubergrits, Florian Hellmeier, Dominik Neumann, Viorel Mihalef, Mehmet A. Gulsun, Marcello Chinali, Aurelio Secinaro, Kilian Runte, Stephan Schubert, Felix Berger, Titus Kuehne, Anja Hennemuth, and Marcus Kelm. Patient-specific requirements and clinical validation of MRI-based pressure mapping: A two-center study in patients with aortic coarctation. Journal of Magnetic Resonance Imaging, 49(1):81–89, 2019.
- [19] Hojin Ha, Guk Bae Kim, Jihoon Kweon, Young-Hak Kim, Namkug Kim, Dong Hyun Yang, and Sang Joon Lee. Multi-venic acquisition of four-dimensional phase-contrast mri to improve precision of velocity field measurement. Magnetic resonance in medicine, 75(5):1909–1919, 2016.
- [20] Hojin Ha, John-Peder Escobar Kvitting, Petter Dyverfeldt, and Tino Ebbers. Validation of pressure drop assessment using 4D flow MRI-based turbulence production in various

- shapes of aortic stenoses. Magnetic Resonance in Medicine, 81(2):893–906, February 2019.
- [21] Hojin Ha, Jonas Lantz, Magnus Ziegler, Belen Casas, Matts Karlsson, Petter Dyverfeldt, and Tino Ebbers. Estimating the irreversible pressure drop across a stenosis by quantifying turbulence production using 4d flow mri. Scientific reports, 7:46618, 2017.
- [22] Henrik Haraldsson, Sarah Kefayati, Sinyeob Ahn, Petter Dyverfeldt, Jonas Lantz, Matts Karlsson, Gerhard Laub, Tino Ebbers, and David Saloner. Assessment of reynolds stress components and turbulent pressure loss using 4d flow mri with extended motion encoding. Magnetic resonance in medicine, 79(4):1962–1971, 2018.
- [23] Andrea D. Holton, Edward G. Walsh, Brigitta C. Brott, Ramakrishna Venugopalan, Bradley Hershey, Yasushi Ito, Alan Shih, Roy Koomullil, and Andreas S. Anayiotos. Evaluation of in-stent stenosis by magnetic resonance phase-velocity mapping in nickel-titanium stents. Journal of Magnetic Resonance Imaging, 22(2):248–257, 2005.
- [24] P. R. Hoskins. Accuracy of maximum velocity estimates made using Doppler ultrasound systems. The British journal of radiology, 69(818):172–177, 1996.
- [25] Sebastian B. S. Krittian, Pablo Lamata, Christian Michler, David A. Nordsletten, Jelena Bock, Chris P. Bradley, Alex Pitcher, Philip J. Kilner, Michael Markl, and Nic P. Smith. A finite-element approach to the direct computation of relative cardiovascular pressure from time-resolved MR velocity data. Medical Image Analysis, 16(5):1029–1037, July 2012.
- [26] David N. Ku. Blood flow in arteries. Annu Rev Fluid Mech, 29(1):399–434, 1997.
- [27] A. Linke and C. Merdon. Pressure-robustness and discrete Helmholtz projectors in mixed finite element methods for the incompressible Navier–Stokes equations. Computer Methods in Applied Mechanics and Engineering, 311:304–326, November 2016.
- [28] Michael Markl, Frandics P. Chan, Marcus T. Alley, Kris L. Wedding, Mary T. Draney, Chris J. Elkins, David W. Parker, Ryan Wicker, Charles A. Taylor, and Robert J. Herfkens. Time-resolved three-dimensional phase-contrast MRI. Journal of Magnetic Resonance Imaging: An Official Journal of the International Society for Magnetic Resonance in Medicine, 17(4):499–506, 2003.
- [29] Michael Markl, Alex Frydrychowicz, Sebastian Kozerke, Mike Hope, and Oliver Wieben. 4D flow MRI. JRMI, 36(5):1015–1036, 2012.
- [30] David Marlevi, Hojin Ha, Desmond Dillon-Murphy, Joao F Fernandes, Daniel Fovargue, Massimiliano Colarieti-Tosti, Matilda Larsson, Pablo Lamata, C Alberto Figueroa, Tino Ebbers, et al. Non-invasive estimation of relative pressure in turbulent flow using virtual work-energy. Medical Image Analysis, 60:101627, 2020.

- [31] David Marlevi, Bram Ruijsink, Maximilian Balmus, Desmond Dillon-Murphy, Daniel Fovargue, Kuberan Pushparajah, Cristóbal Bertoglio, Massimiliano Colarieti-Tosti, Matilda Larsson, Pablo Lamata, C. Alberto Figueroa, Reza Razavi, and David A. Nord-sletten. Estimation of Cardiovascular Relative Pressure Using Virtual Work-Energy. Scientific Reports, 9(1), December 2019.
- [32] Cristian Montalba, Jesus Urbina, Julio Sotelo, Marcelo E. Andia, Cristian Tejos, Pablo Irarrazaval, Daniel E. Hurtado, Israel Valverde, and Sergio Uribe. Variability of 4D flow parameters when subjected to changes in MRI acquisition parameters using a realistic thoracic aortic phantom. Magnetic resonance in medicine, 79(4):1882–1892, 2018.
- [33] Phillip Moore. Mri-guided congenital cardiac catheterization and intervention: The future? Catheterization and cardiovascular interventions, 66(1):1–8, 2005.
- [34] Abbas Nasiraei-Moghaddam, Geoffrey Behrens, Nasser Fatourae, Ramesh Agarwal, Eric T. Choi, and Amir A. Amini. Factors affecting the accuracy of pressure measurements in vascular stenoses from phase-contrast MRI. Magnetic Resonance in Medicine: An Official Journal of the International Society for Magnetic Resonance in Medicine, 52(2):300–309, 2004.
- [35] Elizabeth Nett, Kevin Johnson, Alex Frydrychowicz, Alejandro Muñoz, Eric Schrauben, Christopher Francois, and Oliver Wieben. Four-dimensional phase contrast mri with accelerated dual velocity encoding. Journal of Magnetic Resonance Imaging, 35(6):1462–1471, 2012.
- [36] S. B. Pope. Turbulent Flows. Cambridge University Press, Cambridge ; New York, 2000.
- [37] Reza Razavi, Vivek Muthurangu, Sanjeet R Hegde, and Andrew M Taylor. Mr-guided cardiac catheterization. In Clinical Cardiac MRI, pages 513–538. Springer, 2005.
- [38] Fabian Rengier, Michael Delles, Joachim Eichhorn, Yoo-Jin Azad, Hendrik von Tengg-Kobligk, Julia Ley-Zaporozhan, Rüdiger Dillmann, Hans-Ulrich Kauczor, Roland Unterhinninghofen, and Sebastian Ley. Noninvasive 4D pressure difference mapping derived from 4D flow MRI in patients with repaired aortic coarctation: Comparison with young healthy volunteers. The international journal of cardiovascular imaging, 31(4):823–830, 2015.
- [39] Eugénie Riesenkampff, Joao Filipe Fernandes, Sebastian Meier, Leonid Goubergrits, Siegfried Kropf, Stephan Schubert, Felix Berger, Anja Hennemuth, and Titus Kuehne. Pressure fields by flow-sensitive, 4D, velocity-encoded CMR in patients with aortic coarctation. JACC: Cardiovascular Imaging, 7(9):920–926, 2014.
- [40] Julio Sotelo, Jesús Urbina, Israel Valverde, Joaquín Mura, Cristián Tejos, Pablo Irarrazaval, Marcelo E. Andia, Daniel E. Hurtado, and Sergio Uribe. Three-dimensional

- quantification of vorticity and helicity from 3D cine PC-MRI using finite-element interpolations. Magnetic resonance in medicine, 79(1):541–553, 2018.
- [41] Julio Sotelo, Jesus Urbina, Israel Valverde, Cristian Tejos, Pablo Irrarrázaval, Marcelo E. Andia, Sergio Uribe, and Daniel E. Hurtado. 3D quantification of wall shear stress and oscillatory shear index using a finite-element method in 3D CINE PC-MRI data of the thoracic aorta. IEEE transactions on medical imaging, 35(6):1475–1487, 2016.
- [42] Julio A Sotelo, Israel Valverde, Philipp B Beerbaum, Gerald F Greil, Tobias Schaeffter, Reza Razavi, Daniel E Hurtado, Sergio Uribe, and Carlos A Figueroa. Pressure gradient prediction in aortic coarctation using a computational-fluid-dynamics model: validation against invasive pressure catheterization at rest and pharmacological stress. Journal of Cardiovascular Magnetic Resonance, 17(S1):Q78, 2015.
- [43] H. Švihlová, J. Hron, J. Málek, K. R. Rajagopal, and K. Rajagopal. Determination of pressure data from velocity data with a view toward its application in cardiovascular mechanics. Part 1. Theoretical considerations. International Journal of Engineering Science, 2016.
- [44] Roger Temam. Navier-Stokes Equations: Theory and Numerical Analysis, volume 343. American Mathematical Soc., 2001.
- [45] Jesús Urbina, Julio A. Sotelo, Daniel Springmüller, Cristian Montalba, Karis Letelier, Cristián Tejos, Pablo Irrarrázaval, Marcelo E. Andia, Reza Razavi, and Israel Valverde. Realistic aortic phantom to study hemodynamics using MRI and cardiac catheterization in normal and aortic coarctation conditions. Journal of Magnetic Resonance Imaging, 44(3):683–697, 2016.
- [46] Carole A. Warnes, Roberta G. Williams, Thomas M. Bashore, John S. Child, Heidi M. Connolly, Joseph A. Dearani, Pedro Del Nido, James W. Fasules, Thomas P. Graham, and Ziyad M. Hijazi. ACC/AHA 2008 Guidelines for the Management of Adults With Congenital Heart Disease: Executive Summary: A Report of the American College of Cardiology/American Heart Association Task Force on Practice Guidelines (Writing Committee to Develop Guidelines for the Management of Adults With Congenital Heart Disease) Developed in Collaboration With the American Society of Echocardiography, Heart Rhythm Society, International Society for Adult Congenital Heart Disease, Society for Cardiovascular Angiography and Interventions, and Society of Thoracic Surgeons. Journal of the American College of Cardiology, 52(23):1890–1947, 2008.

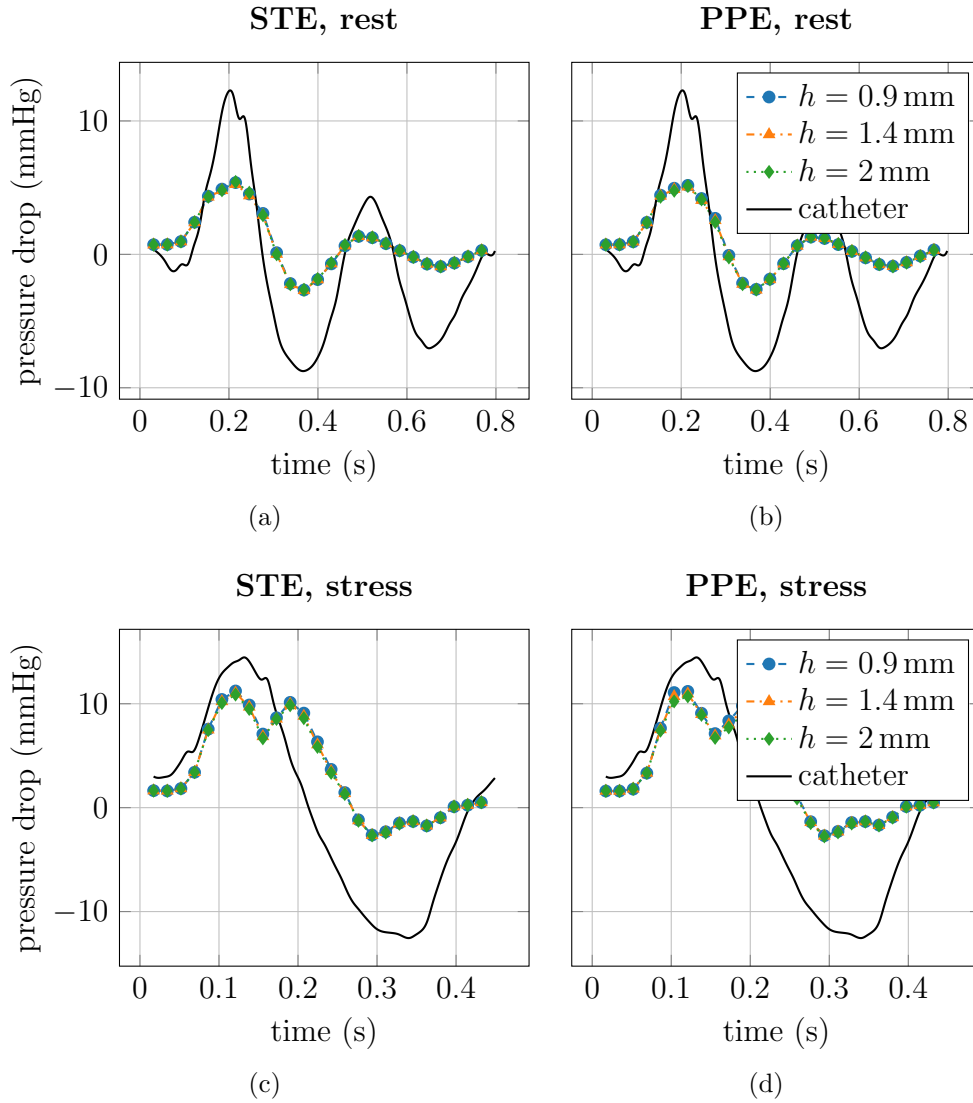


Figure 5: 40% AoCo phantom pressure differences obtained with STE (left column) and PPE (right column) under rest (first row) and stress conditions (second row) using voxel sizes of 0.9 mm, 1.4 mm, 2.0 mm compared to ground truth catheter data.

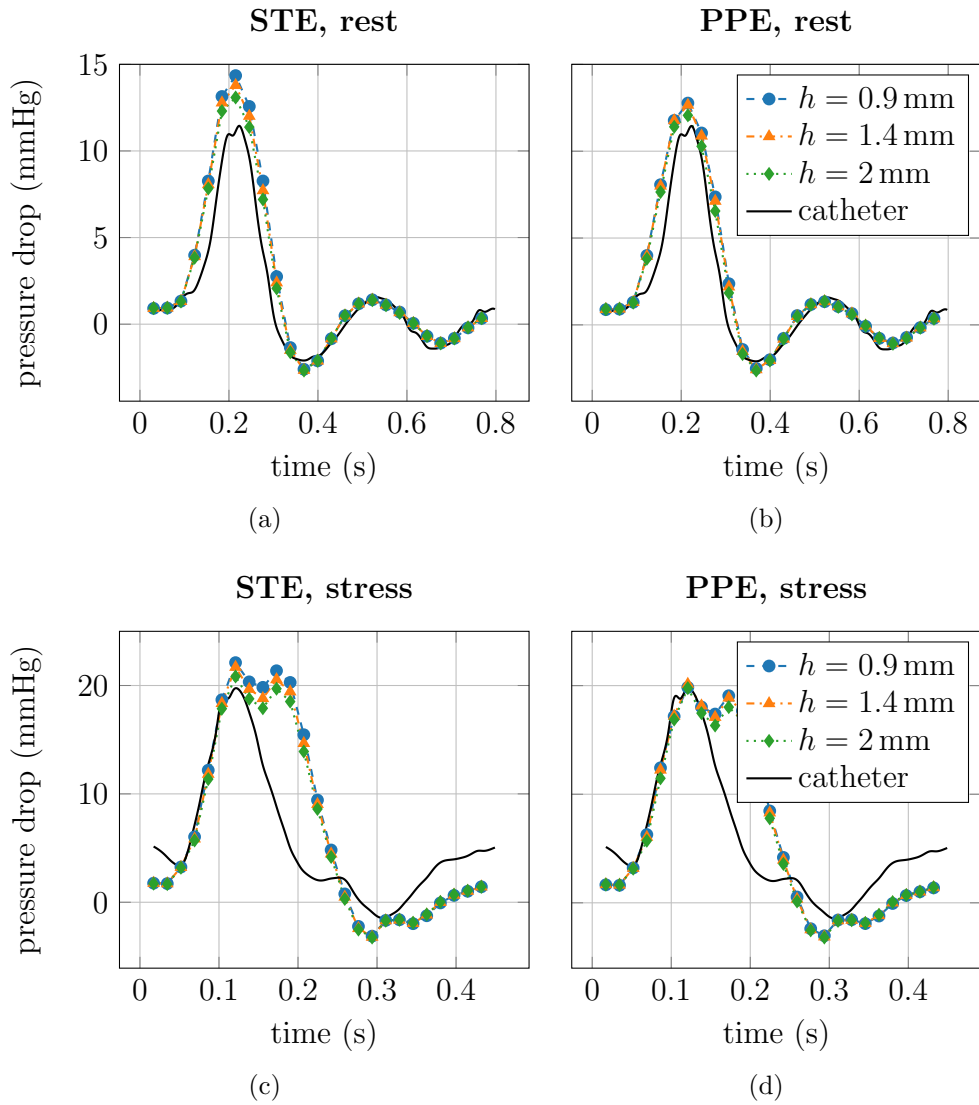


Figure 6: 50% AoCo phantom pressure differences obtained with STE (left column) and PPE (right column) under rest (first row) and stress conditions (second row) using voxel sizes of 0.9 mm, 1.4 mm, 2.0 mm compared to ground truth catheter data.

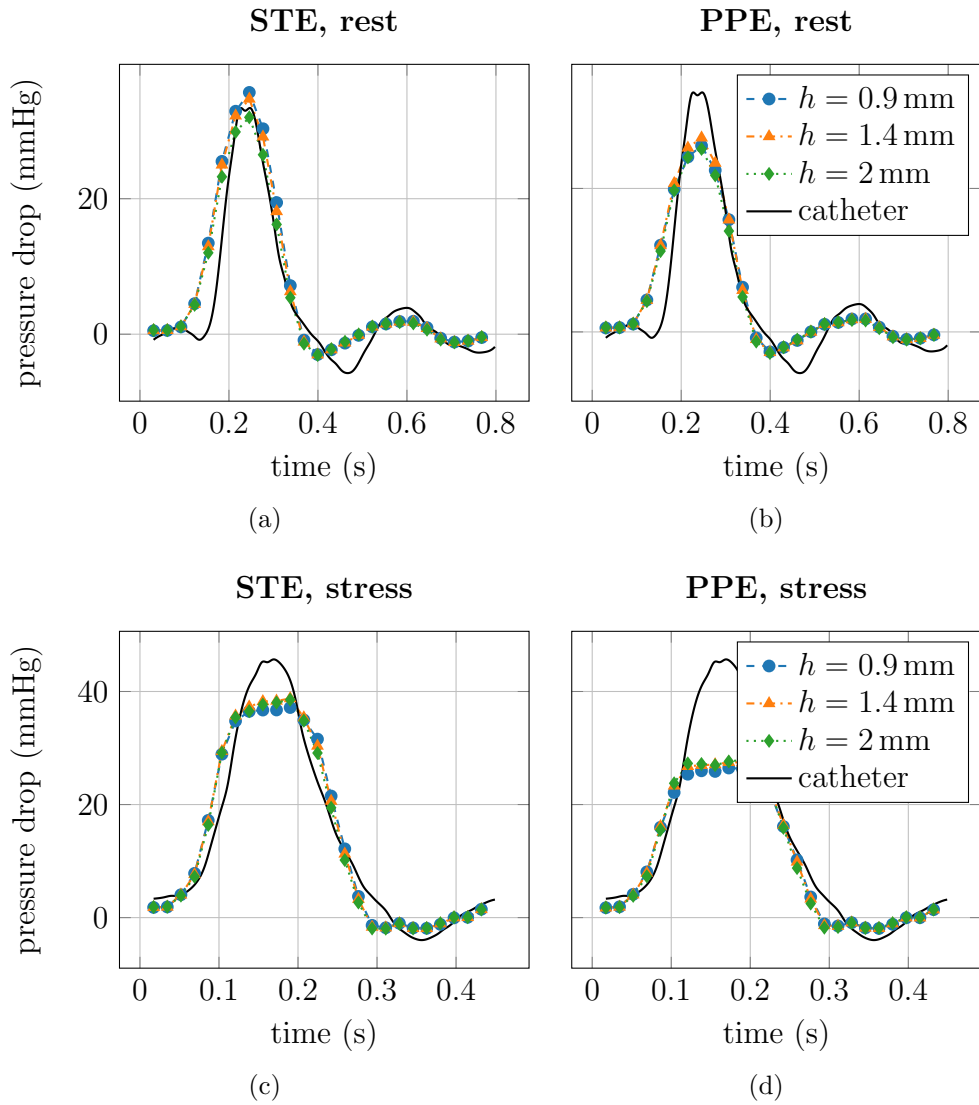
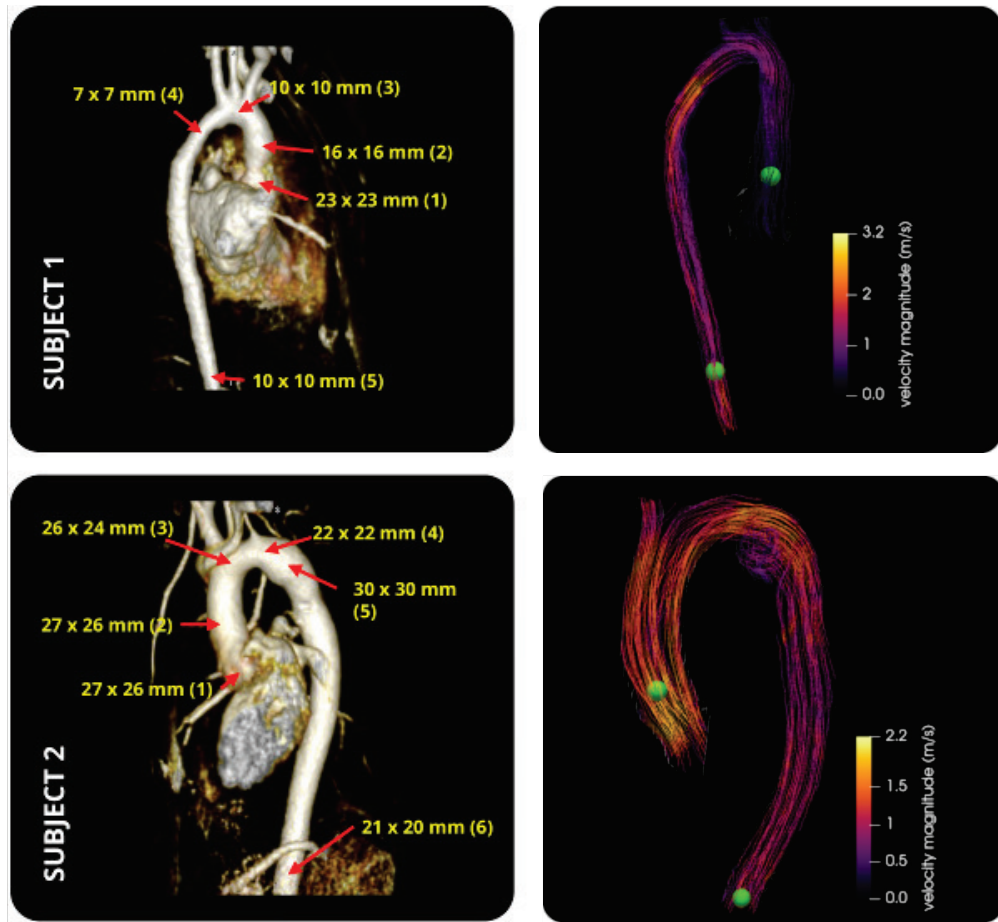
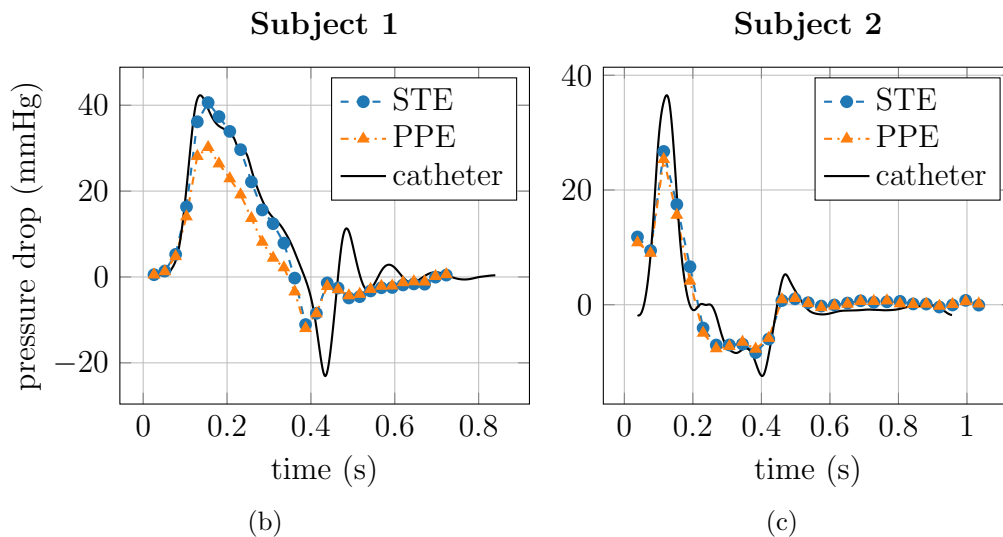


Figure 7: 60% AoCo phantom pressure differences obtained with STE (left column) and PPE (right column) under rest (first row) and stress conditions (second row) using voxel sizes of 0.9 mm, 1.4 mm, 2.0 mm compared to ground truth catheter data.



(a)



(b)

(c)

Figure 8: Patient data: (a) left column: angiographic images obtained using contrast agent, for both subjects, with annotations of the cross-sectional dimensions in terms of the widths in millimeters in two perpendicular directions; right column: streamlines of 4D Flow at peak, spheres indicate locations of pressure difference calculation. (b), (c) pressure differences computed with STE and PPE compared to catheter data